

Scaling in river corridor widths depicts organization in valley morphology

Chandana Gangodagamage, Elizabeth Barnes, Efi Foufoula-Georgiou*

St. Anthony Falls Laboratory and National Center for Earth-Surface Dynamics, Department of Civil Engineering, University of Minnesota, Minneapolis, USA

Received 13 October 2006; accepted 30 April 2007
Available online 8 August 2007

Abstract

Landscapes have been shown to exhibit numerous scaling laws from Horton's laws to more sophisticated scaling in topography heights, river network topology and power laws in several geomorphic attributes. In this paper, we propose a different way of examining landscape organization by introducing the "river corridor width" (lateral distance from the centerline of the river to the left and right valley walls at a fixed height above the water surface) as one moves downstream. We establish that the river corridor width series, extracted from 1 m LIDAR topography of a mountainous river, exhibit a rich multiscale statistical structure (anomalous scaling) which varies distinctly across physical boundaries, e.g., bedrock versus alluvial valleys. We postulate that such an analysis, in conjunction with field observations and physical modeling, has the potential to quantitatively relate mechanistic laws of valley formation to the statistical signature that underlying processes leave on the landscape. Such relations can be useful in guiding field work (by identifying physically distinct regimes from statistically distinct regimes) and advancing process understanding and hypothesis testing.

© 2007 Elsevier B.V. All rights reserved.

Keywords: River corridor widths; Valley morphology; Hillslope processes; Landscape organization; Multiscaling; Multifractals

1. Introduction

"Why are scaling laws of such distinguished importance? The answer is that scaling laws never appear by accident. They always manifest a property of the phenomenon of basic importance ... This behavior should be discovered, if it exists, and its absence should also be recognized." — Barenblatt (2003).

A piece of landscape can be analyzed in several ways. One way is to analyze the statistical properties of the

topography heights $z(x,y)$ and related attributes, such as, local gradients and curvatures. Another way is to extract the channelized paths of the topography and study the topological structure of the ordered river network. The former method examines the vertical structure of the topography, while the latter studies the planar dissection of the topography. Here, we introduce a different approach for examining landscapes focusing on the "river corridor width" (RCW) as one moves along the river. The river corridor width is extracted by "flooding" the river at a certain height D_0 above the water surface and recording the left and right distance to the valley walls measured from the centerline of the river and orthogonal to this centerline (see Fig. 1). We denote this function by $V_L(x; D_0)$ and $V_R(x; D_0)$, where L and R stand for the left and right side, respectively, looking downstream, x is the

* Corresponding author. Tel.: +1 612 626 0369; fax: +1 612 624 4398.

E-mail address: efi@umn.edu (E. Foufoula-Georgiou).

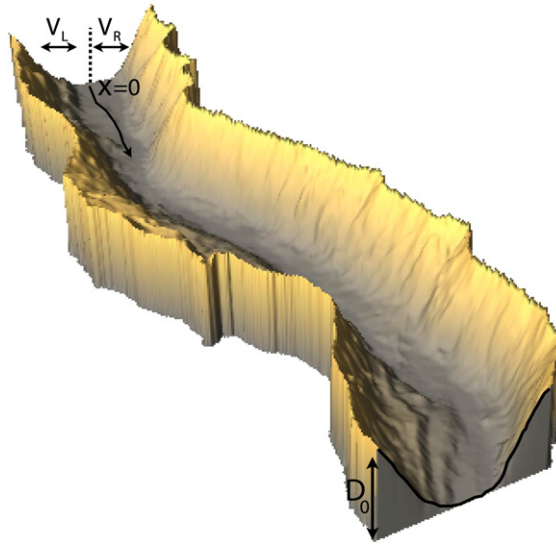


Fig. 1. River corridor width at depth D_0 above the water surface to the left and right of the river centerline, $V_L(x; D_0)$ and $V_R(x; D_0)$, respectively, where x is the distance measured along the river from the basin outlet $x=0$.

distance measured along the river from the basin outlet $x=0$, and D_0 is the depth above the water level.

This particular definition of “river corridor width” is different from the definition of “valley width” used in other studies. For example, [Montgomery \(2002\)](#) defined valley width as the total ridgetop-to-ridgetop width of valley-spanning cross-sections orthogonal to the valley centerline. Montgomery’s study aimed to understand how valley morphometry scales with drainage area in glaciated versus unglaciated valleys for the purpose of arriving at a process-based classification of valley morphology. Thus, valley widths were extracted in his study from several cross-sections throughout the basin and were selected to avoid the influence of tributary valleys. In our study, we follow the valley as we move downstream the mainstream and record the river corridor width to the left and right side of the river centerline as we “flood” the valley to different heights D_0 (see [Fig. 1](#)). The scope of our analysis is not to extract regional scaling characteristics but instead to quantify the detailed statistical structure of the valley morphology as one follows the river downstream with the eventual goal of relating this statistical structure to the processes responsible for valley formation. The river corridor width series is extracted from high resolution airborne altimetry (LIDAR) topography data at cross-sections 1 m apart as we move downstream along the river and, thus, depicts landscape organization down to the meter scale.

The small-scale fluctuations of the river corridor width series are interpreted to have resulted from the complex, and often interacting, processes forming valleys, including hillslope transport, mass wasting, terraces, debris flows,

landsliding and the interactions with the streams. The question we pose is whether the river corridor width series exhibit any distinct statistical scaling properties, and in particular any form of statistical organization across a range of scales, i.e., scale invariance or self-similarity. The methodology of analysis heavily borrows from current state-of-the-art methodologies for analyzing turbulent velocity fluctuations. We demonstrate how spectral analysis provides a limited, or partial, characterization of the multiscale structure of the river corridor width series. The use of a rigorous multifractal analysis unravels a rich scaling structure and, in particular, a deviation from scale invariance and presence of strong intermittency, the so-called anomalous scaling. These findings are revealing and call for further analysis of the statistical signature that valley forming processes leave on the landscapes in diverse geomorphic environments and also along tributaries of nested sub-basins. It is postulated that distinct statistical signatures identified from high resolution topography can be further explored towards (a) discriminating among different valley morphologies, (b) suggesting the nature of the underlying mechanisms responsible for valley formation, and (c) guide field work and data collection efforts for the purpose of advancing modeling and hypothesis testing.

2. Study area and extraction of river corridor width series

The South Fork Eel River basin is located in northern California and has a drainage area of 351 km^2 (see [Fig. 2](#)). Its relief is approximately 500 m. The mainstream of the

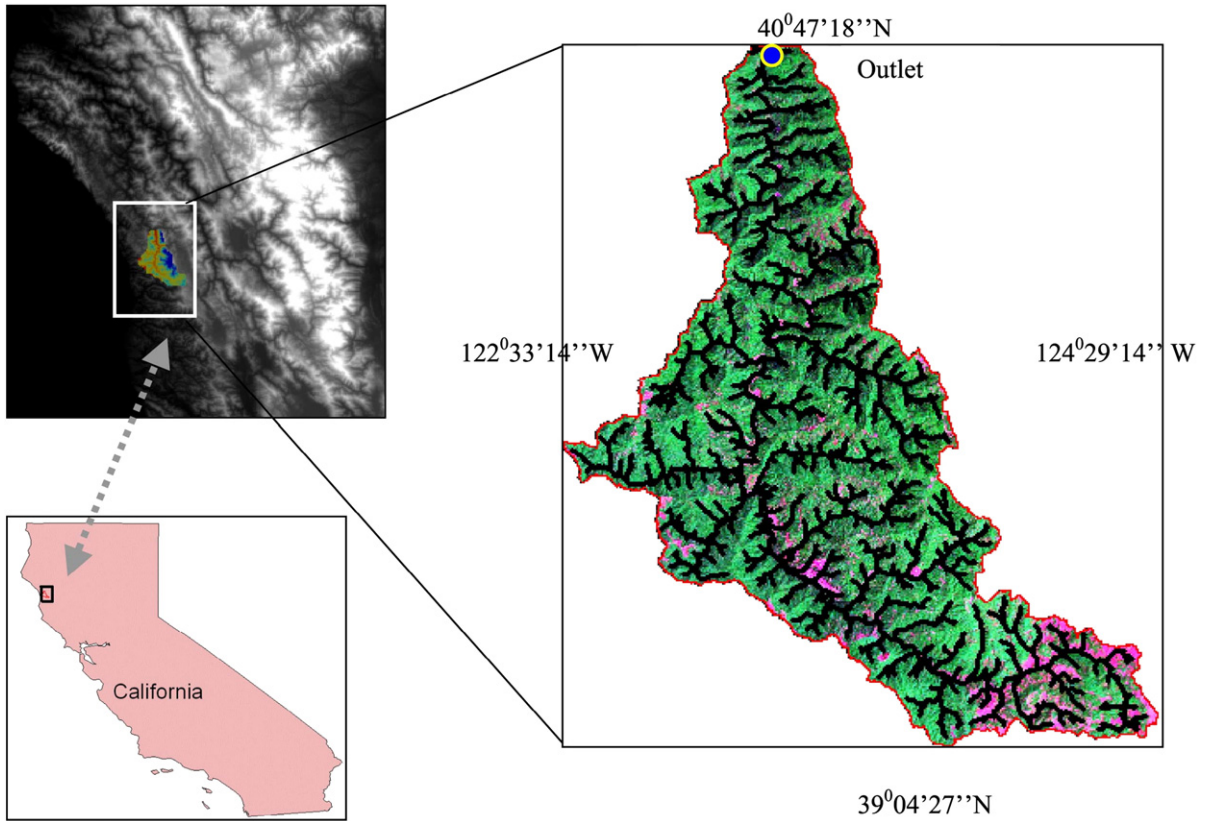


Fig. 2. Location of the South Fork Eel River basin (351 km²) in California. The panel on the right shows the stream network superimposed on Landsat GeoCover (Bands 7, 4, 2) image of the basin.

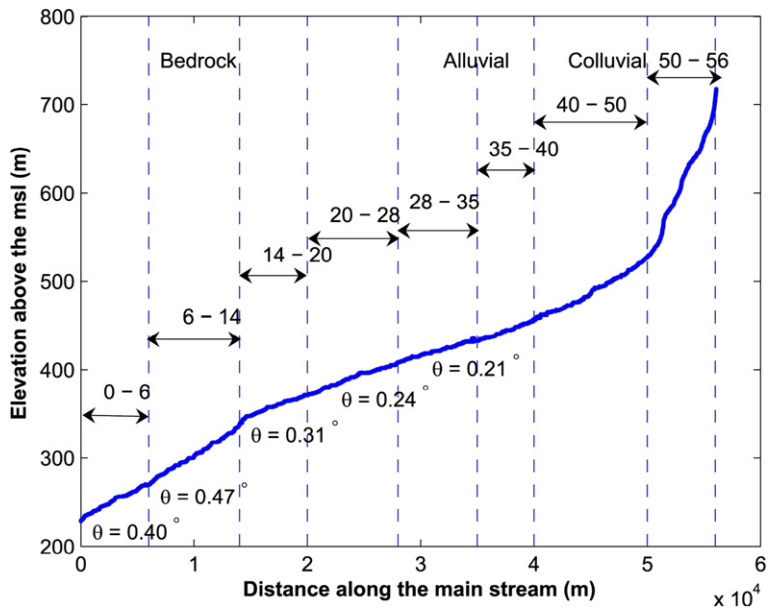


Fig. 3. Longitudinal profile along the main channel of the South Fork Eel River basin. The main channel is divided into eight segments (see discussion in text and Table 1) whose respective along-channel slopes (in degrees) and distances from the outlet (in km) are shown above.

Table 1

Segments along the mainstream of the Eel River ($x=0$ denotes the outlet of the basin, see Fig. 1) and the scaling properties of their right and left river corridor width (RCW) series

Distance from outlet (km)	Along stream slope (°)	Side of the corridor (Left/Right)	Spectral slope	Scaling range (m)	Scaling range (octaves)	Holder exponent $\langle H \rangle$	(h_{\min}, h_{\max})	c_1	c_2
0 < x < 6	0.40	Right	1.27	5.0–36.8	2.5–5.2	0.45	(−0.1, 1.18)	0.45	0.07
		Left	1.36	9.2–64	3.0–6.0	0.47	(0.02, 1.02)	0.50	?
6 < x < 14	0.47	Right	1.63	9.2–56	3.2–5.8	0.51	(0, 1.30)	0.51	?
		Left	1.45	8.6–56	3.1–5.8	0.49	(0.1, 1.22)	0.48	0.02
14 < x < 20	0.31	Right	1.18	8.0–56.0	3.0–5.8	0.29	(−0.1, 1.20)	0.32	0.13
		Left	1.19	9.8–36.8	3.3–5.2	0.39	(0.0, 1.07)	0.41	0.25
20 < x < 28	0.24	Right	1.21	8.0–64	3.0–6.0	0.58	(0.1, 1.10)	0.59	0.05
		Left	1.28	16.0–128	4.0–7.0	0.22	(−0.1, 0.60)	0.23	0.17
28 < x < 35	0.21	Right	1.41	8.0–128	3.0–7.0	0.81	(0.0, 2.00)	1.00	0.38
		Left	1.43	8.0–128	3.0–7.0	0.76	(0.0, 1.60)	0.77	0.10

The reported Hölder exponent $\langle H \rangle$ is estimated from the CWT multifractal analysis, the (h_{\min}, h_{\max}) from the WTMM multifractal analysis, and c_1, c_2 from the cumulant analysis. Notice the pronounced multifractality ($c_2 \neq 0$) of the RCW series for some segments (e.g. both left and right sides of 14–20 km and left side only of the 20–28 km segment.) Also note the different values of $\langle H \rangle$ (and c_1) suggesting a smoother RCW series for the 0–14 km steep-sloped, bedrock stretch and a much rougher RCW series for the milder-sloped, alluvial 14–28 km stretch.

basin has a length of approximately 56 km and fairly steep along-the-channel slopes (see Fig. 3 and Table 1). We have subdivided this channel reach into eight smaller sub-reaches according to slope and other morphologic characteristics, such as the presence of tributaries. These eight segments were then analyzed separately. The idea was to avoid mixing different physical regimes at the expense of classifying the reaches in more detail than necessary. The presence of similar statistical properties could then be used to group reaches into fewer categories (and this was indeed the case from our analysis). Following Montgomery (2002), valleys have been classified as bedrock, alluvial and colluvial (see Fig. 3). For vegetation and other

geomorphological characteristics of this region, the reader is referred to Power (1992) and Seidl and Dietrich (1992).

For this watershed, 1 m topography data from airborne altimetry (LIDAR) is available from which we extracted the cross-sections of the ridgetop-to-ridgetop valleys perpendicular to the river centerline every 1 m along the mainstream. Then, at specified depths D_0 above the water level, the distances from the centerline of the river to the left and right valley walls were recorded. The analysis was performed at depth $D_0=5$ m and $D_0=10$ m for the whole river. In this paper we report the analysis of the $D_0=5$ m river corridor widths for the very steep 35 km stretch from the outlet to the divide. The 20 km stretch close to the

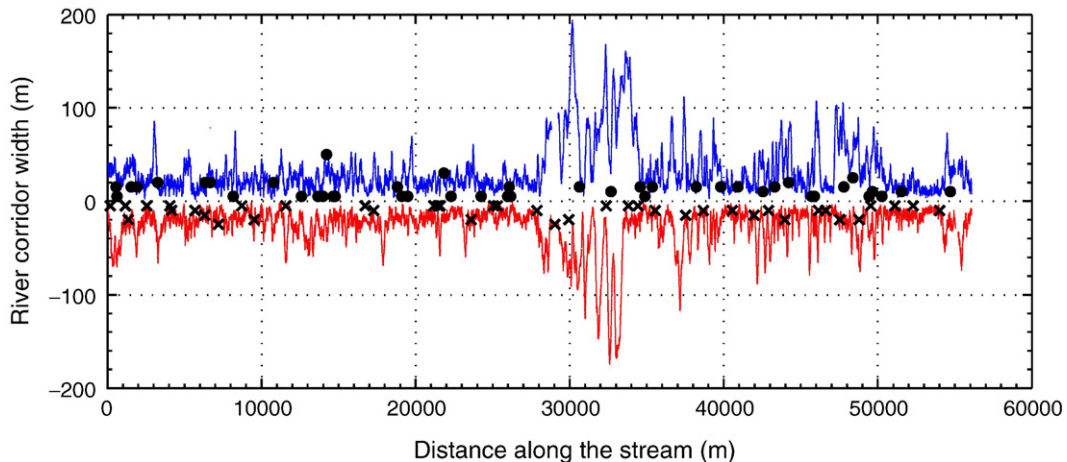


Fig. 4. River corridor widths for the mainstream of the South Fork Eel River (56 km in length) extracted at a depth $D_0=5$ m: top (+Y) is at the right side and bottom (−Y) is at the left side of the river as we travel downstream. Dots (●) and crosses (×) indicate the location of tributaries joining the mainstream at the right and left sides respectively. (See text for more details.)

divide did not show a clear scaling signature and requires further analysis.

Fig. 4 displays the left and right river corridor width (RCW) series for the whole 56 km mainstream and also indicates the location of the tributary junctions. To provide an indication of the “significance” of each tributary, we have positioned the marks at a vertical distance proportional to the drainage area of each tributary. Specifically, the 89 tributaries have been grouped into 10 categories based on the contributing drainage areas. These groups are then scaled such that the smallest contributing area of 1 km^2 corresponds to (is plotted at) a RCW of 5 m, and the

largest area of 152 km^2 corresponds to a RCW of 50 m (See Fig. 4).

Fig. 5 shows a magnification of the river corridor width series for the 0–6 km river stretch and the detailed topography and location of this stretch within the whole basin. It also associates selected values in the river corridor width with the locations on the topographic map. Finally, Fig. 6 shows the river corridor width series for the 20–28 km alluvial stretch. As will be discussed later, this stretch exhibits a rich multiscale structure in its RCW series and a pronounced asymmetry between the left and right sides. This asymmetry (not visually

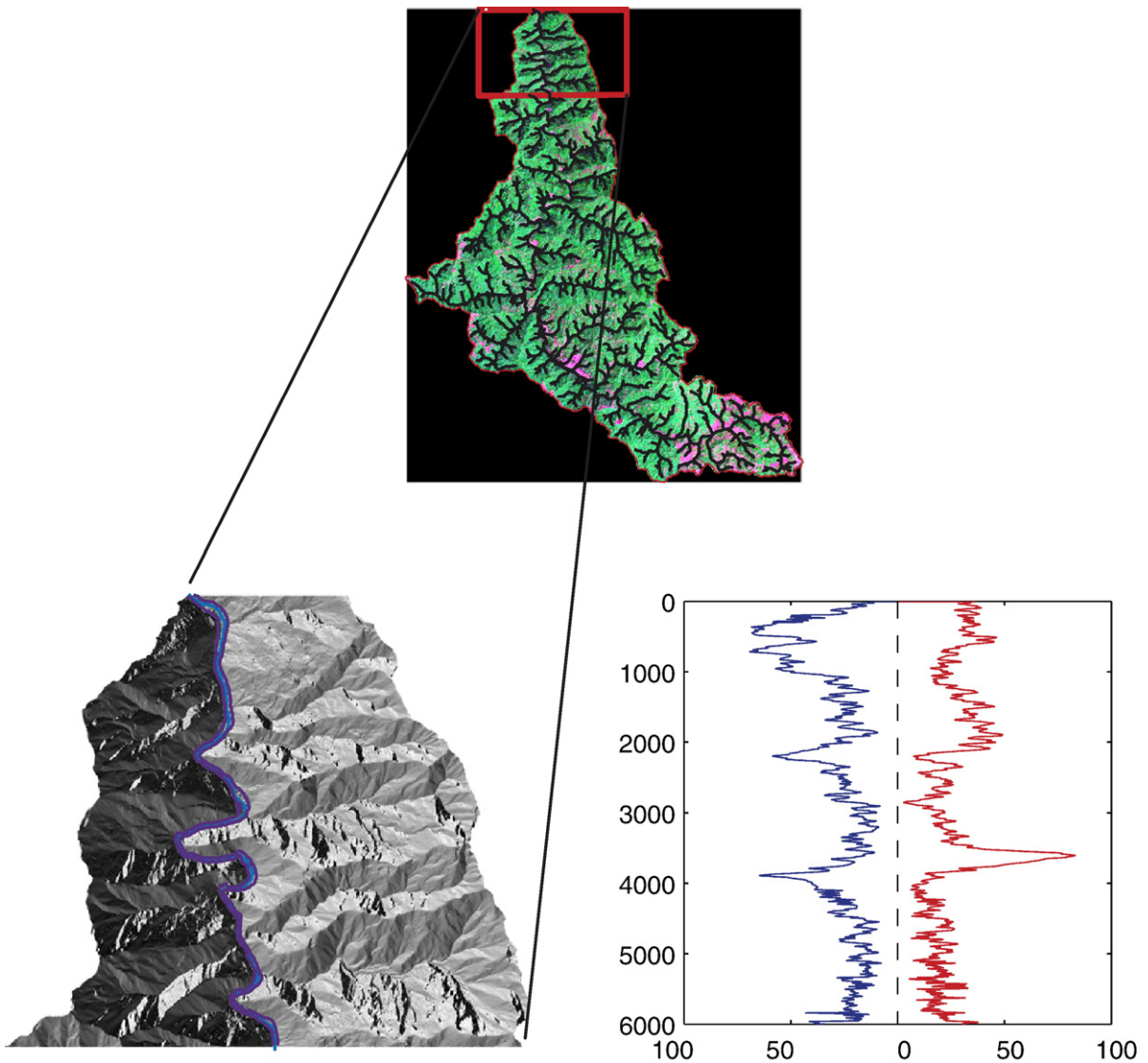


Fig. 5. The 0–6 km bedrock stretch of the South Fork Eel River basin. Selected values of river corridor width are associated with their locations on the topographic map.

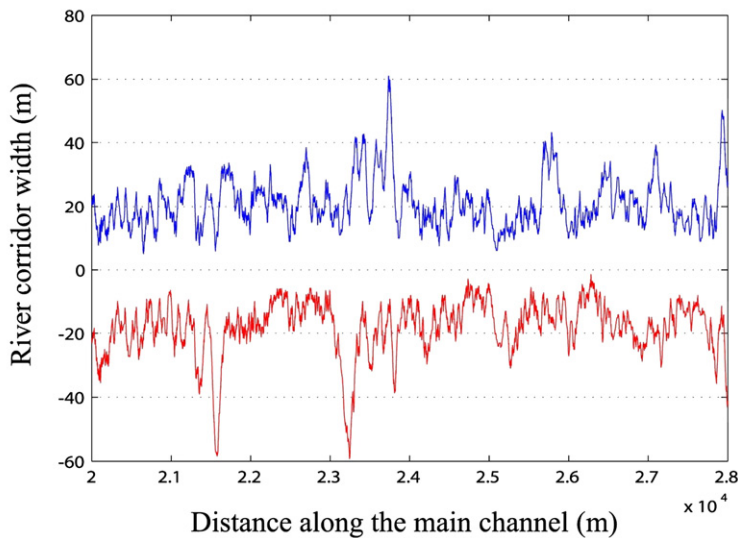
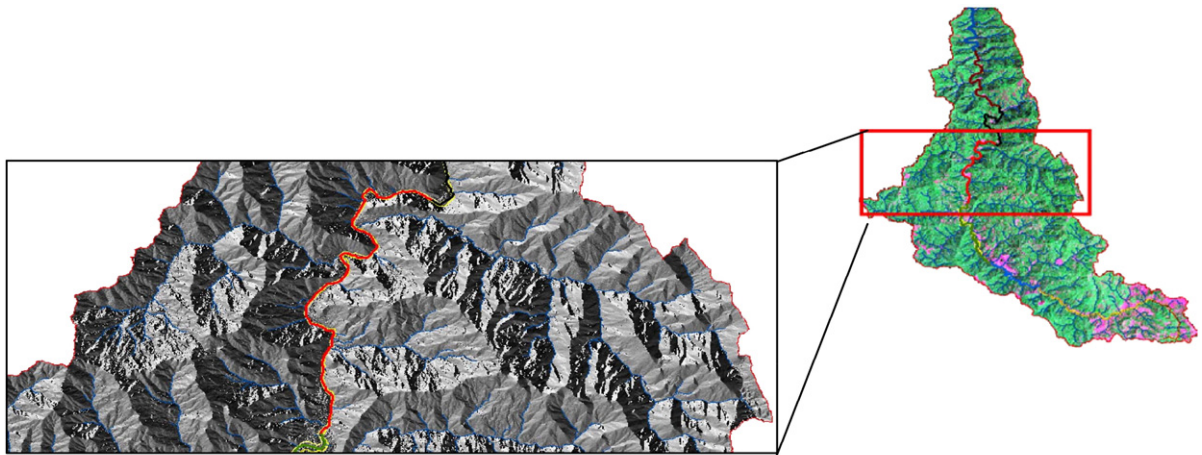


Fig. 6. The 20–28 km stretch of the South Fork Eel River basin main channel (top panel). The bottom panel shows the right (top series) and left (bottom series) river corridor widths extracted from this 8 km stretch at depth $D_0=5$ m. This stretch exhibits a high asymmetry in the statistical scaling properties of its left and right valley geometries; although not apparent visually, the right side is much “smoother” than the left side (see Table 1 and discussion in text). This suggests different valley forming processes in each side of the mainstream, with much more localized processes in the left side.

apparent from Fig. 6, but clearly depicted by the multiscale analysis) can be seen as suggesting different valley-forming processes for each side.

3. Fourier analysis of river corridor width series

A commonly used tool to explore the energy distribution of a signal across frequencies (or scales) is the power spectrum. The power spectra of the left and right RCW series of the five segments analyzed are shown in Fig. 7. First, we observe the presence of a log–log linearity over a significant range of scales with an abrupt break of scaling at a scale of approximately 10 m except

for the 0–6 km stretch which does not exhibit a pronounced scaling break. For scales smaller than approximately 10 m (wavenumber larger than 10^{-1} m^{-1}) a significant increase of energy (variability) is present. This is interpreted as the result of noise in the LIDAR data that shows up as concentrated energy at characteristic scales of the order of 5–10 m (the so-called “acne” in the bare soil LIDAR extracted topography.) This scale of 10 m, below which the LIDAR data are not globally interpretable (although locally they do depict smaller than 10 m variability), represents the “effective resolution” of these topography data and has also been documented from a break in the

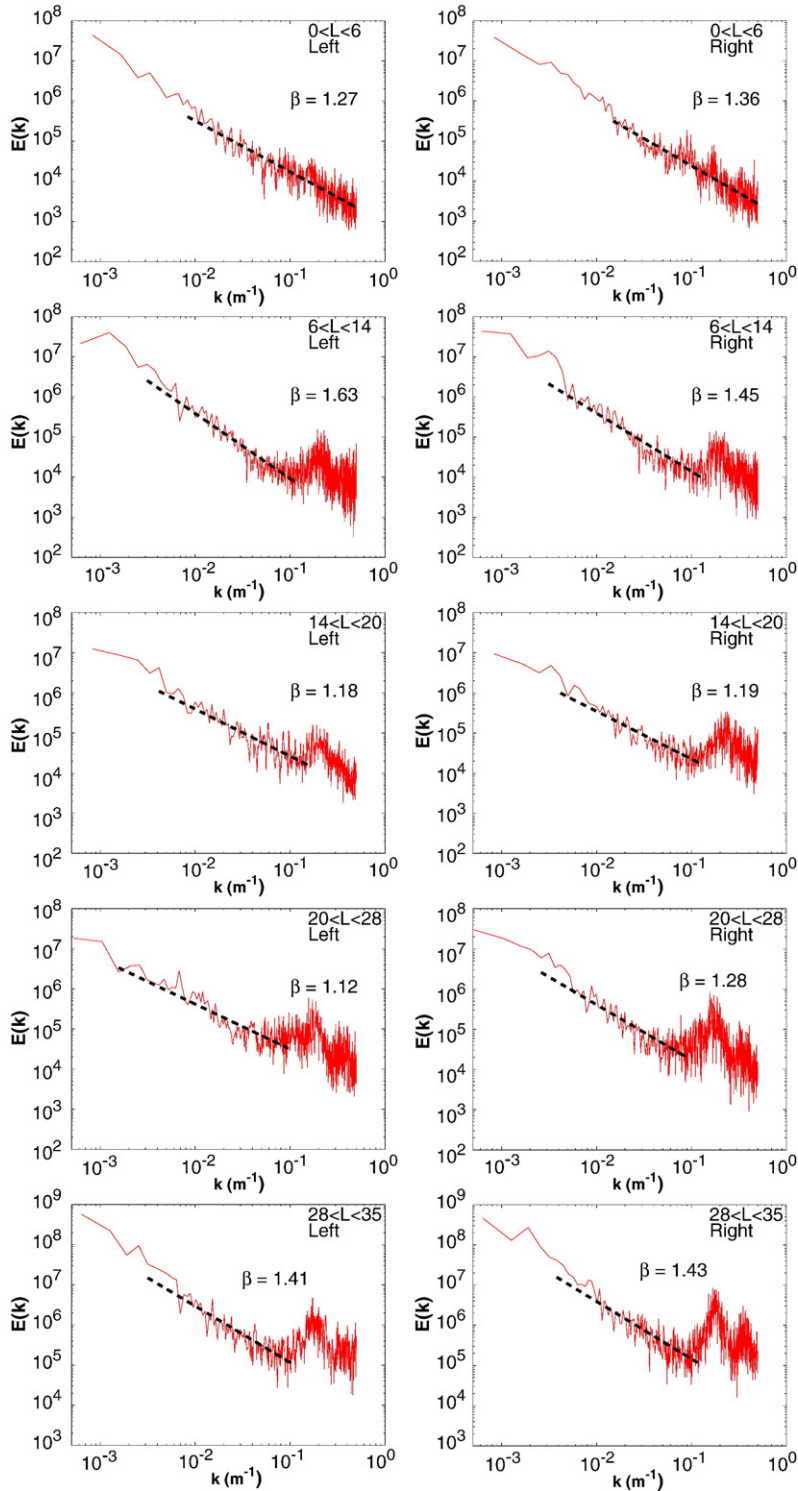


Fig. 7. Power spectra of the river corridor widths (at 5 m above water level) for the five segments along the mainstream of the South Fork Eel River basin. The dotted black lines give the power law fits, $E(k)=k^{-\beta}$. The horizontal axis represents frequency k , in m^{-1} .

multiscale statistical properties of basin-wide curvature pdfs at approximately the same scale (Lashermes and Foufoula-Georgiou, 2007).

It is well known that the presence of large-scale features with sharp edges in a process can be misinterpreted in the usual Fourier spectrum as energy

coming from distinct small-scale features, because the Fourier analysis cannot distinguish between the two. Thus, we do not know from Fig. 7 whether the log–log linearity in the spectrum within the scaling range is the result of uniformly distributed high-energy fluctuations over the whole support of the signal or a richer preferential and localized energy distribution. The former is the hallmark of scale-invariance, implying a spatially homogeneous distribution of abruptly high values within the support of the signal (arising from a homogenous energy transferring mechanism), while the latter is indicative of a break-down of scale invariance, implying a localized intermittent distribution of abruptly large values within the signal (probably arising from a spatially inhomogeneous energy transferring mechanism). In turbulence, the realization that the statistical moments of turbulent velocity fluctuations grow faster as the scale becomes smaller, prompted the replacement of the global Fourier-based analysis of Kolmogorov (K41 theory, Kolmogorov, 1941) with the local multifractal formalism analysis of Parisi and Frisch (1985).

The multifractal formalism aims to characterize the very abrupt local fluctuations in the signal using the so-called multifractal (MF) spectrum. The MF spectrum, or spectrum of singularities $D(h)$, describes the “richness” of the local irregularities of a function, i.e., abrupt local fluctuations, in terms of local singularities characterized via the so-called Hölder exponent h (see Parisi and Frisch, 1985). If singularities are of the same strength throughout the support of the signal (i.e., homogeneously distributed), $D(h)$ receives the value of 1 at a single value of $h=H$ which coincides with the well-known Hurst exponent. If the singularities of various strengths are non-homogeneously spread in the signal (in what turns out to be interwoven fractal sets), however, $D(h)$ is a density function which quantifies the range of the strength of these singularities (h_{\min} to h_{\max}) and the degree of their presence in the signal. In other words, the set of points that exhibit singularity of order h_1 forms a fractal set of dimension $D(h_1)$ and is interwoven with the set of points that exhibit singularity of order h_2 , which forms a fractal set of dimension $D(h_2)$, etc. In the next section, an overview of the multifractal analysis methodologies is presented followed by the results of analysis of the river corridor width series.

4. Multifractal analysis: methodology overview

4.1. Preliminaries

A typical goal of multiscale analysis of a signal $f(x)$ is to characterize how the statistical properties (or the whole

pdf) of the signal changes with the “scale” at which the signal is examined. For that, the statistical moments of the fluctuations of the signal $\delta(x,a)=f(x+a)-f(x)$, at scale (separation distance) a are computed, and the change with scale a is examined. log–log linearity between the statistical moments of order q and scale implies the presence of scaling and the slopes of these lines $\tau(q)$ for different order moments q characterize the nature of scaling. A linear $\tau(q)$ vs. q relationship, i.e., $\tau(q)=q \cdot H$, where H is the Hurst or scaling exponent, implies simple scaling whereas a nonlinear relationship implies a deviation from simple scaling, or multiscaling. In the first case, the single exponent H can be used to obtain the whole pdf at one scale from the pdf at any other scale, while in the second case more than one scaling exponents are needed to renormalize the pdfs across scales (i.e., the tails of the pdfs scale differently than the body). Often, only the second order statistical moment ($q=2$) is checked (second-order structure function or variogram) in which case the single estimated exponent H can be used to renormalize the pdfs only up to second order statistics.

It is instructive to place the above statistical interpretation of mono- or multi-scaling (i.e., looking at how the pdfs renormalize across scales) in the context of an equivalent geometrical interpretation (i.e., what does the scaling really mean about the nature and frequency of very extreme fluctuations in the signal). The multifractal formalism of Parisi and Frisch (1985) connects the statistical and geometrical interpretations intuitively and mathematically, as will be discussed in the next section. Specifically, abrupt fluctuations in the signal (geometrically characterized by the local regularity of the function or the so-called Hölder exponent defined later) occur uniformly or homogeneously throughout the signal in the case of a mono-fractal, while they occur heterogeneously or intermittently in the case of a multifractal. The two imply different mechanisms for how the energy is distributed across scales, i.e., a uniform cascading of energy across scales in the first case, versus a spatially heterogeneous energy cascading in the second case deriving from the presence of intermingled very active and dormant regions of energy transfer.

The processes creating the valley geometry are multiple in nature including hillslope sediment transport, landsliding, mass wasting, tributary influences, etc. and one expects that this can lead to a complex statistical structure of the RCW series. Whether the RCW series exhibit any statistical organization (mono- or multi-scaling) and how this organization is to be statistically and geometrically interpreted, is the scope of this paper. Emphasis is placed on higher order moments which can characterize the local behavior of

abrupt fluctuations as this is considered significant for interpreting the nature of the underlying valley forming processes.

In the rest of this section the mathematical details of the multiscale analysis methodologies we employ are presented. The reader is referred to Venugopal et al. (2006a,b) and the references therein for a more detailed exposition.

4.2. Multifractal formalism

The local singularity of a function $f(x)$ at a point x_0 is characterized by the so-called Hölder exponent $h(x_0)$, defined as the largest exponent such that

$$|f(x) - f(x_0)| \sim C|x - x_0|^{h(x_0)} \quad (1)$$

in the neighborhood of x_0 , i.e. for $|x - x_0| \leq \varepsilon$. A small (large) value of $h(x_0)$ signifies a rough (smooth) behavior of the function $f(x)$ at x_0 . The above definition holds for $0 \leq h \leq 1$ but extension to singularities $h > 1$ (i.e., singularities in the higher-order derivatives of the function) can easily be achieved by filtering out a polynomial of degree higher than one, which is equivalent to working with higher-order increments of the signal. As will be seen later, this filtering can be formally achieved via a wavelet-based formalism (e.g. see Muzy et al., 1991, 1993; or Venugopal et al., 2006a,b).

The singularity spectrum $D(h)$ is defined as

$$D(h) = d_h \{x_0 : h(x_0) = h\} \quad (2)$$

that is, $D(h)$ is the Hausdorff dimension d_h of the set of points x_0 which have Hölder exponent $h(x_0) = h$. Estimating $D(h)$ is the goal of multifractal analysis and the so-called multifractal formalism (e.g. Parisi and Frisch, 1985) allows estimation of $D(h)$ from the statistics of local fluctuations of the signal at different scales a and different locations x_0 , denoted by $\delta(x_0, a)$. One way of determining these fluctuations is via standard first order differences, i.e.,

$$\delta(x_0, a) \equiv f(x_0 + a) - f(x_0). \quad (3)$$

Let us denote the structure functions $S(q, a)$ of the signal as the q th statistical moments of the fluctuations of the signal:

$$S(q, a) = \langle |\delta(x_0, a)|^q \rangle \quad (4)$$

where $\langle \cdot \rangle$ stands for expectation (via spatial averaging). For a multifractal signal

$$S(q, a) \sim a^{\tau(q)} \quad (5)$$

which defines the $\tau(q)$ curve, or spectrum of scaling exponents, indexed by moment order q . The multifractal formalism states that $\tau(q)$ relates to $D(h)$ through a Legendre transform:

$$D(h) = \min_q [qh - \tau(q) + 1]. \quad (6)$$

If the signal under analysis is monofractal, then $\tau(q)$ is linear with respect to the moment order, i.e., $\tau(q) = q \cdot H$ and $D(h)$ receives a single value equal to 1 at the specific value of $h = H$. In contrast, if the singularity spectrum takes on finite values in an interval $[h_{\min}, h_{\max}]$, the scaling exponents $\tau(q)$ define a nonlinear function of q (multifractal signal). The nonlinearity of $\tau(q)$ implies a scale dependence of the dimensionless moments. For example, for a monofractal process it can easily be shown from (5) that the coefficient of variation, $CV = (M_2(a)/M_1^2(a) - 1)^{1/2}$, of the process is independent of scale a , while this is not the case for a multifractal process. The same applies to other dimensionless structure functions such as the coefficients of skewness and kurtosis, $M_3(a)/M_1(a)^{3/2}$ and $M_4(a)/M_2(a)^2$ respectively, where $M_q(a)$ is used to denote $S(q, a)$ (see Mahrt, 1989).

It is understood that an increase of the dimensionless structure functions with decreasing scale is an indication of strong intermittency, i.e., occasional large gradients which enhance the higher order moments at small scales (break-down of scale invariance). This empirical observation, documented from long series of wind-tunnel turbulence data, is what lead to the development of the multifractal formalism in turbulence (e.g. Parisi and Frisch, 1985) and shed new light into how energy is cascaded in a turbulent field, typically very intensely in localized regions and less so in other (dormant) regions. As it will be seen in the next section, the river corridor widths are also found to exhibit such a multifractal behavior (break of scale-invariance), suggesting a rich local structure of energy dissipation in the valley-forming processes.

4.3. Wavelet-based MF formalism

While one could confine themselves to using structure functions in (4) as computed from the standard first order differences of the signal as defined in (3), it is often advantageous to use “generalized differences” defined via wavelet filtering. One advantage is that wavelets allow the analysis of non-stationary signals. By choosing an appropriate wavelet (i.e., wavelets with a high number of vanishing moments), polynomial trends of increasing order can be filtered out from the

signal and accurately characterize the local behavior of a function without danger of having this behavior masked by the large-scale trends (e.g. Jaffard, 1989; Mallat and Hwang, 1992). Another advantage of wavelets is their natural ability to depict sharp edges or discontinuities from a signal (e.g. Muzy et al., 1994; Mallat, 1998) and, thus, better characterize the statistical nature of singularities. In addition, as we explain below, a wavelet-based multifractal formalism allows one to work with the maxima of the wavelet coefficients (the so-called wavelet transform modulus maxima; WTMM) and, thus, extend the structure function analysis to negative moments q (which are necessary for computation of the right limb of the $D(h)$ spectrum.) Such an extension also allows access to the whole spectrum of singularities, including $h > 1$ which is not possible by using the standard definition of fluctuations (3).

A wavelet-based multifractal formalism uses as fluctuations

$$\delta(x_0, a) = c(x_0, a) = \int_R \psi_{x_0, a}(x) f(x) dx \tag{7}$$

where $\psi_{x_0, a}(x)$ is a scale-dilated and shifted version of the mother wavelet $\psi_0(x)$, i.e.,

$$\psi_{x_0, a}(x) = \frac{1}{|a|} \psi_0\left(\frac{x - x_0}{a}\right). \tag{8}$$

The so-defined $S(q, a)$ in (4) is called the partition function or generalized structure function. The use of a wavelet with N vanishing moments, i.e., $\int x^K \psi_x(x) dx = 0$, for $(0 \leq K \leq N - 1)$ and $\int x^N \psi_0(x) dx \neq 0$, allows for the removal of a degree- N polynomial trend (see Mallat, 1998). This is important if first order differences do not completely remove trends in the data, for then the standard multifractal analysis will fail.

A standard wavelet, and the one used in this analysis, is the first and second order derivative of a Gaussian function, i.e.,

$$g^{(N)}(x) = \frac{d^{(N)}}{dx^{(N)}} \left(e^{-\frac{x^2}{2}} \right) \tag{9}$$

which has been extensively used as a smooth generalization of N -th order increments to study the behavior of fractal functions (e.g. Muzy et al., 1994; Arneodo et al., 1995).

From the Legendre transform (6), in the case of a continuously differentiable $\tau(q)$, it follows that

$$q = \frac{dD(h)}{dh}. \tag{10}$$

Thus, the right limb of $D(h)$, where $(dD(h)/dh < 0)$, can only be estimated from the negative moments ($q < 0$) of the fluctuations. Computing negative moments of pdfs that have mass concentrated at zero (such as the pdfs of fluctuations), however, leads to divergence. To be able to take negative moments and estimate the complete singularity spectrum, Muzy et al. (1991, 1994) proposed to use the wavelet transform modulus maxima (WTMM) method, i.e., concentrate on the lines formed by following the maxima of the wavelet coefficients across scales and, thus, following the same singularity from the lowest scale to higher and higher scales. For details on this estimation, the reader is referred to the original publications (Muzy et al., 1991, 1993; Arneodo et al., 1998; and also Venugopal et al., 2006a,b).

4.4. Cumulant analysis

Cumulant analysis presents an efficient method of estimating the multifractal nature of a process and quantifying it in terms of a small number of parameters (e.g. Arneodo et al., 1998; and Delour et al., 2001). This method relies on a Taylor series expansion of $\tau(q)$, leading to

$$\tau(q) = \sum_{p \geq 1} (-1)^{p-1} \frac{c_p}{p!} q^p, q \rightarrow 0. \tag{11}$$

From the above equation one observes that a non-zero value of c_2 (also called the intermittency coefficient) implies deviation from monofractality and explicitly characterizes the richness of the spatial inhomogeneity of very high fluctuations. In fact, the value of c_2 formally relates to the change of the variance of the Hölder exponents (strength of singularities) with scale, (e.g. see Venugopal et al., 2006a,b, Appendix B and references therein) and, thus, characterizes the second order statistics of the singularities. Indeed, a quadratic approximation of $\tau(q)$

$$\tau(q) \cong c_1 q - c_2 \frac{q^2}{2}, q \rightarrow 0 \tag{12}$$

which corresponds to a quadratic approximation of $D(h)$

$$D(h) \cong 1 - \frac{(h - c_1)^2}{2c_2}, h \rightarrow c_1 \tag{13}$$

is a commonly used model of multifractality (the so-called log-normal model in turbulence).

The coefficients c_p can be estimated from the statistical cumulants $C(p, a)$ of order p of the logarithms of the absolute value of the wavelet coefficients $|c(x_0, a)|$ at a given scale, a , (Eq. (7)), or from the logs of the

WTMM coefficients. For details see Delour et al. (2001) and Venugopal et al. (2006a,b). For instance, for $p=1,2$

$$C(1, a) = \frac{a}{n(a)} \sum_{x_0} \ln|c(x_0, a)| \cong a_1 + c_1 \ln(a) \quad (14)$$

$$C(2, a) = \frac{a}{n(a)} \sum_{x_0} [\ln|c(x_0, a)| - C(1, a)]^2 \cong a_2 - c_2 \ln(a). \quad (15)$$

Thus, linear regression of $C(p, a)$ versus $\ln(a)$ allows for an easy estimation of c_p and only two linear regressions (giving estimates of c_1 and c_2) characterize the multifractality up to a quadratic approximation of the $\tau(q)$ function.

In the next section, the continuous wavelet-based multifractal analysis, the WTMM analysis, and the cumulant analysis are applied to the RCW series for a detailed characterization of the series' multifractal structure. It is emphasized that one of the goals of this study is to be able to depict the signature that mechanistic processes leave on the valleys, and thus accuracy and high discriminatory power of the multifractal characterization methodologies is a necessity.

5. Multifractal analysis: results

The river corridor widths of the five different segments from 0 to 35 km (see Fig. 3) have been analyzed using the multifractal formalism. It was found that the coefficient of variation (which characterizes the first two moments only) for these series shows a dependence on scale (see Fig. 8)

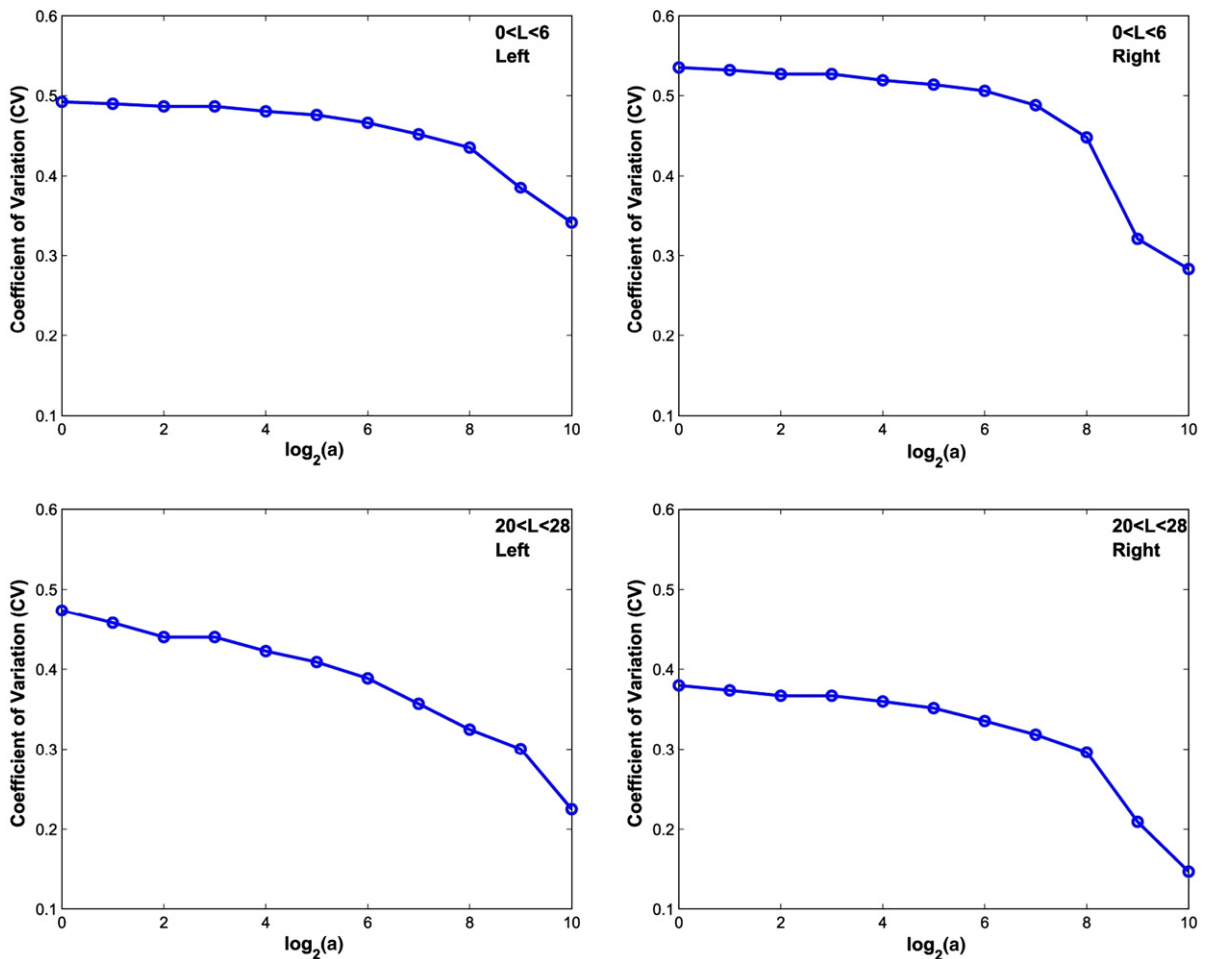


Fig. 8. Coefficient of variation of the river corridor widths as a function of scale for the two segments (0–6 km and 20–28 km) along the mainstream of the South Fork Eel River. The dependence on scale implies deviation from monoscaling. Similar plots were found for all other segments.

and, as expected, an increase as the scale decreases. This is an indication of deviation from monofractality and prompts analysis of higher order moments via the proposed wavelet-based multifractal formalism.

The top panels of Fig. 9 show the partition functions for $q=0$ to 3 (computed in intervals of $q=0.1$, but displayed in intervals of 0.5) for the right and left side river corridor widths of the first ($x=0-6$ km) segment of the South Fork Eel River. The analysis was performed

using the continuous wavelet transform (CWT) with wavelet $g^{(2)}$ and $g^{(3)}$ i.e., the second and third order derivative of the Gaussian, (Eq. (9)). As can be seen, log–log linearity can be assumed between a range of scales as marked in Fig. 9. This range of scales corresponds to approximately 5 m to 40 m for the right side valley and 9 m to 64 m for the left side valley (see Table 1). Fitting straight lines to all moments and computing the slopes results in the $\tau(q)$ curves (middle

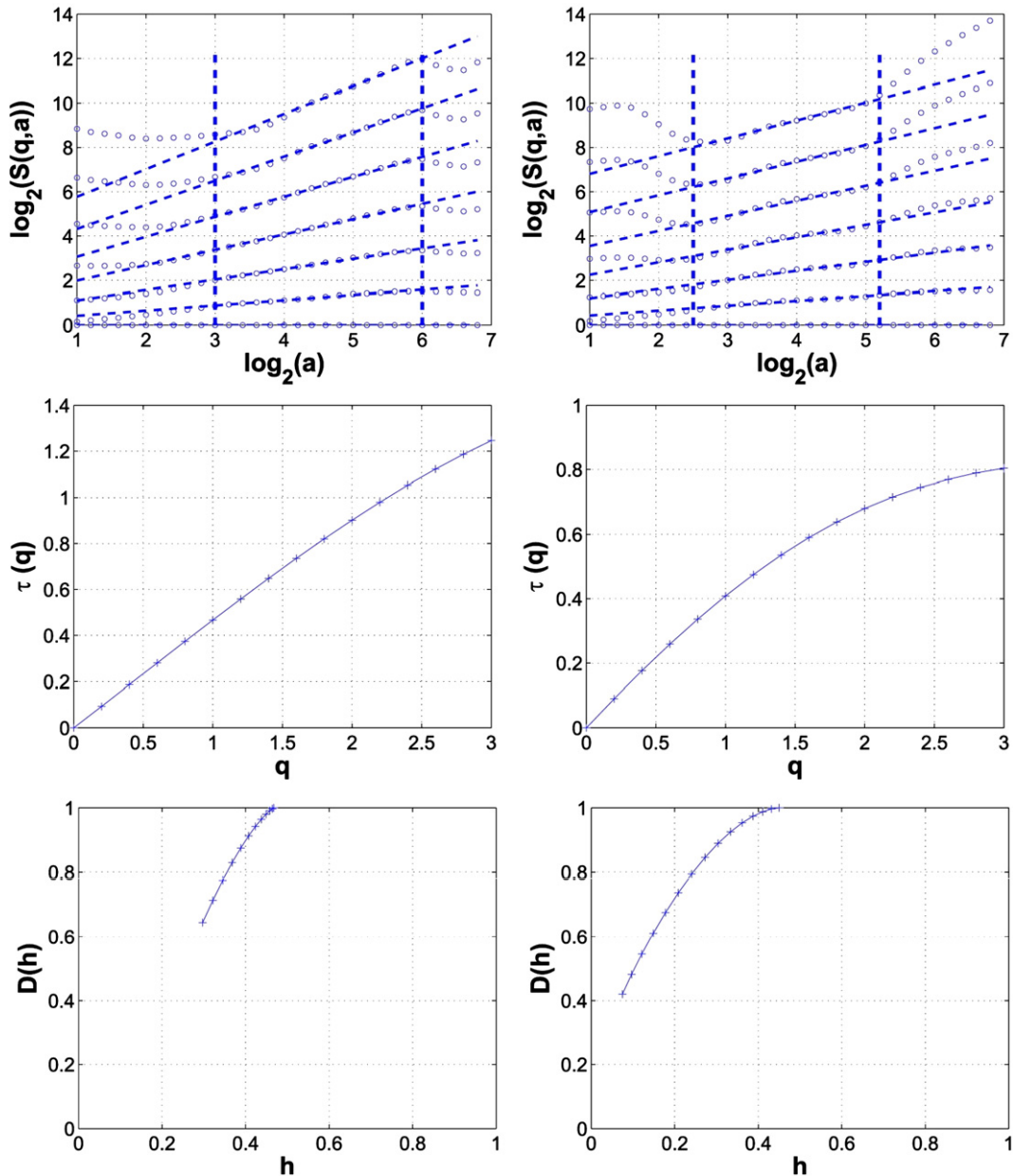


Fig. 9. River reach of 0–6 km, partition functions of order $q=0.0$ to 3.0 using CWT (top), scaling exponent spectrum (middle) and singularity spectrum (bottom) for the left and right river corridor width series at depth $D_0=5$ m. The scaling range of the left corridor (3.2 to 6.0 octaves) and the right corridor (2.5 to 5.2 octaves) is indicated by the dashed vertical lines (see Table 1 for the scaling range in meters).

panels of Fig. 9), and via the Legendre transform results in the $D(h)$ curves (bottom panels of Fig. 9). The nonlinearity of the $\tau(q)$ curves is noted, as was expected from the coefficient of variation dependence on scale, signifying again a deviation from monofractality and, thus, the presence of singularities of various strengths, as quantified in the $D(h)$ spectra. Similar analysis has been performed for all other series. For example, see Fig. 10 for the segment of 20–28 km. A summary of the

scaling ranges for each river reach and the estimates of the most prevailing Hölder exponent $\langle H \rangle$ (the value of h corresponding to the max value of $D(h)$) is given in Table 1.

As was discussed in the previous section, using continuous wavelet transforms does not allow characterization of the right part of the spectrum of singularities. To estimate the full $D(h)$ curve, the WTMM-based multifractal analysis was also applied to these series

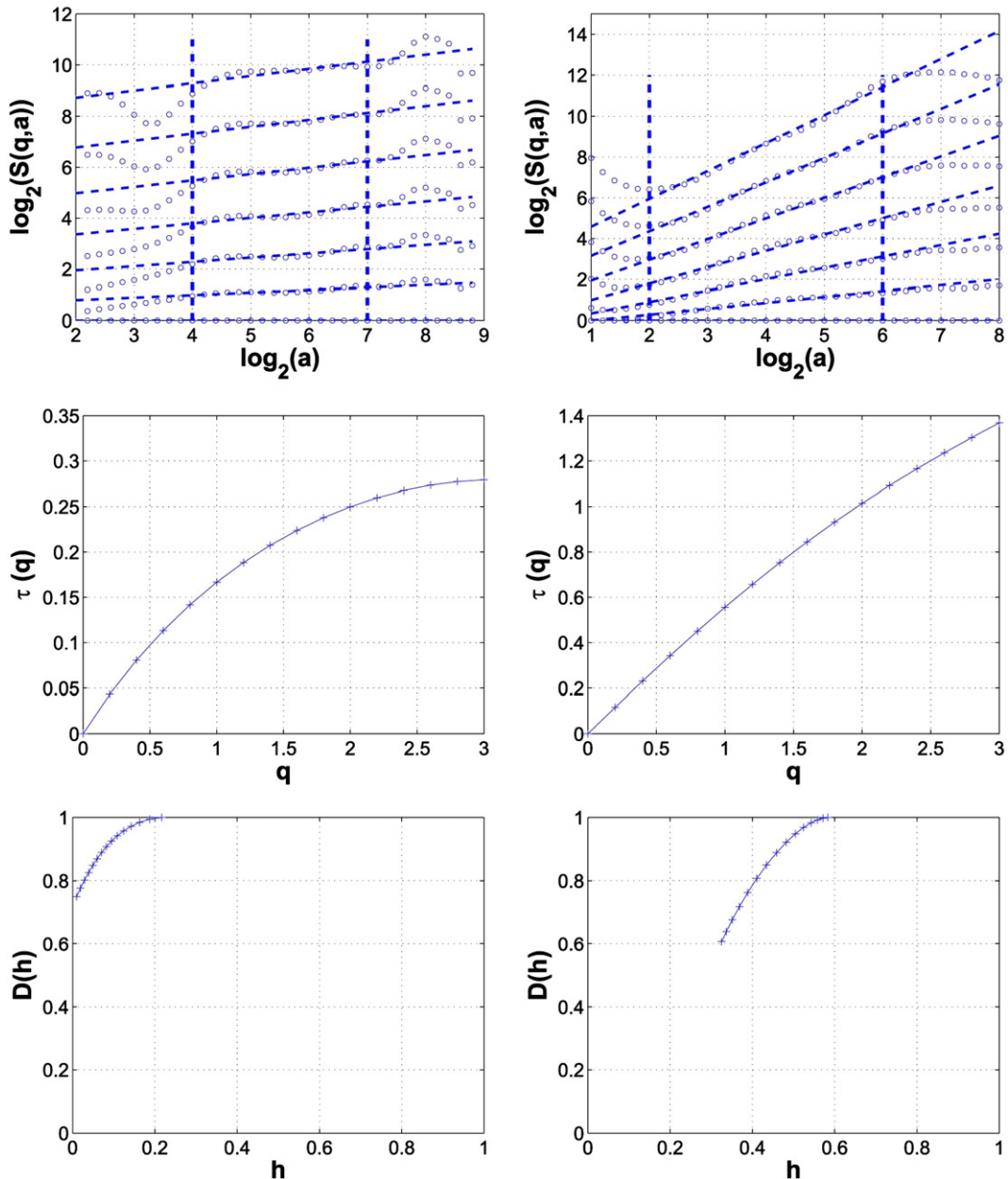


Fig. 10. Same as Fig. 9 but for the 20–28 km river reach. See Table 1 for scaling range.

which allows estimation of the statistical moments for negative order q . Fig. 11 shows the analysis for the 0–6 km river stretch. The top panels display the partition function for $q=-3$ to $+3$ (in increments of 0.5) and the fitted log–log linear lines within the scaling range previously reported. The middle panel shows the $\tau(q)$ curves and the bottom panels the complete $D(h)$ curve. On the same figures, we have superimposed the estimated $\tau(q)$ and $D(h)$ curves from the CWT analysis.

Some small differences in the estimation of the left part of $D(h)$ curve between the CWT and WTMM methods is noted, but also the ability of WTMM to provide an estimate of the right part of $D(h)$ is appreciated. The WTMM analysis was repeated for all series and the values of h_{\min} and h_{\max} (depicting the width of the spectrum of singularities) are summarized in Table 1. It is noted that for several sites, h_{\max} was found to be greater than one. This emphasizes the need to adopt a wavelet-

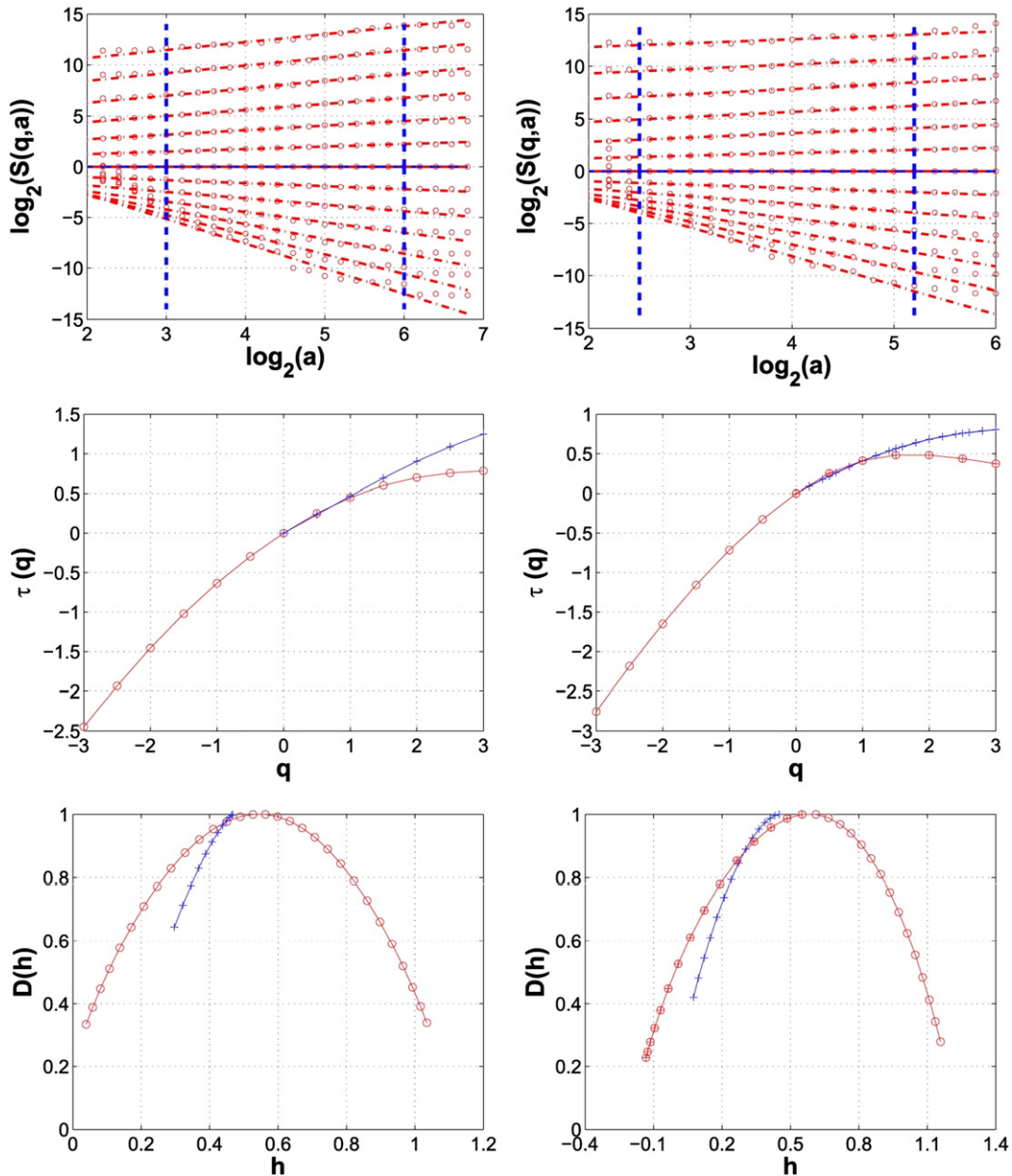


Fig. 11. River reach of 0–6 km, partition functions of order $q=-3.0$ to 3.0 using WTMM (top), scaling exponent spectrum $\tau(q)$ (middle) and singularity spectrum $D(h)$ (bottom) for the left and right river corridor width series at depth $D_0=5$ m using CWT (+) and WTMM (O).

based multifractal analysis, as the standard structure function analysis based on first order increments cannot resolve singularities of order greater than one.

Having established the presence of multifractality, the next step in the analysis is to explicitly estimate the c_1 and c_2 coefficients using the cumulant analysis method. It is expected that c_1 will be very close to the value of $\langle H \rangle$ estimated from the CWT partition function method, but the particular interest is to estimate c_2 which concisely characterizes the intermittency of each series.

Fig. 12 shows the first two cumulants for the right and left river corridor width series of segment 0–6 km. As expected, a log–log linear relationship in $C(1, a)$ vs. $\ln(a)$ yields an estimate of c_1 very close to the estimate of $\langle H \rangle$ obtained from the partition function approach (see Table 1). The $C(2, a)$ vs. $\ln(a)$ plots show a non-zero slope for the right valley (consistent with the wide spectrum of singularities displayed in the bottom right panels of Figs. 9 and 11) and an almost zero slope for the left valley (consistent with the more narrow spectrum of singularities for this series) as seen in Figs. 9 and 11

bottom left panels. Similar analysis was performed for all other series and the estimates of c_1 and c_2 are summarized in Table 1.

It is instructive to display in Fig. 13 the cumulant analysis of the right and left river corridor width series of the segment 20–28 km for which a significant left-to-right asymmetry was noted from the Hölder exponent $\langle H \rangle$ (see Table 1). Specifically, the left side valley was found to have much “rougher” fluctuations (smaller $\langle H \rangle$) than the right side valley (larger $\langle H \rangle$). It is pleasing to see that the cumulant analysis is able to further quantify this asymmetry (see values of c_1 in Table 1) and also depict an asymmetry in intermittency. Specifically, the left side RCW series shows a much more intermittent structure (larger c_2 value) and indicates the presence of more complex or interacting mechanisms forming this side of the valley. From the 20–28 km river segment, shown in Fig. 6, it is noted that from the RCW series themselves, one cannot visually depict the significant statistical differences we were able to establish using the proposed methodologies, although by close inspection of the high resolution topography,

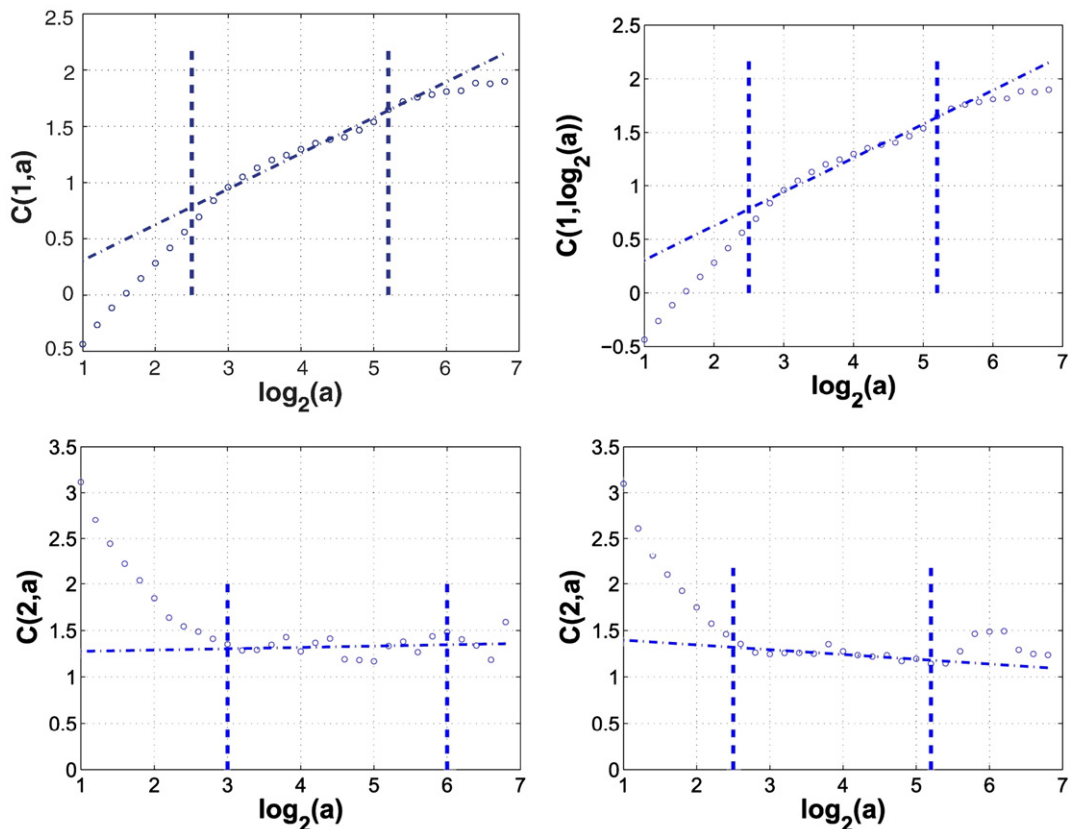


Fig. 12. Cumulant analysis of the left and right river corridor width series of reach 0–6 m, to estimate parameters c_1 and c_2 in Table 1.

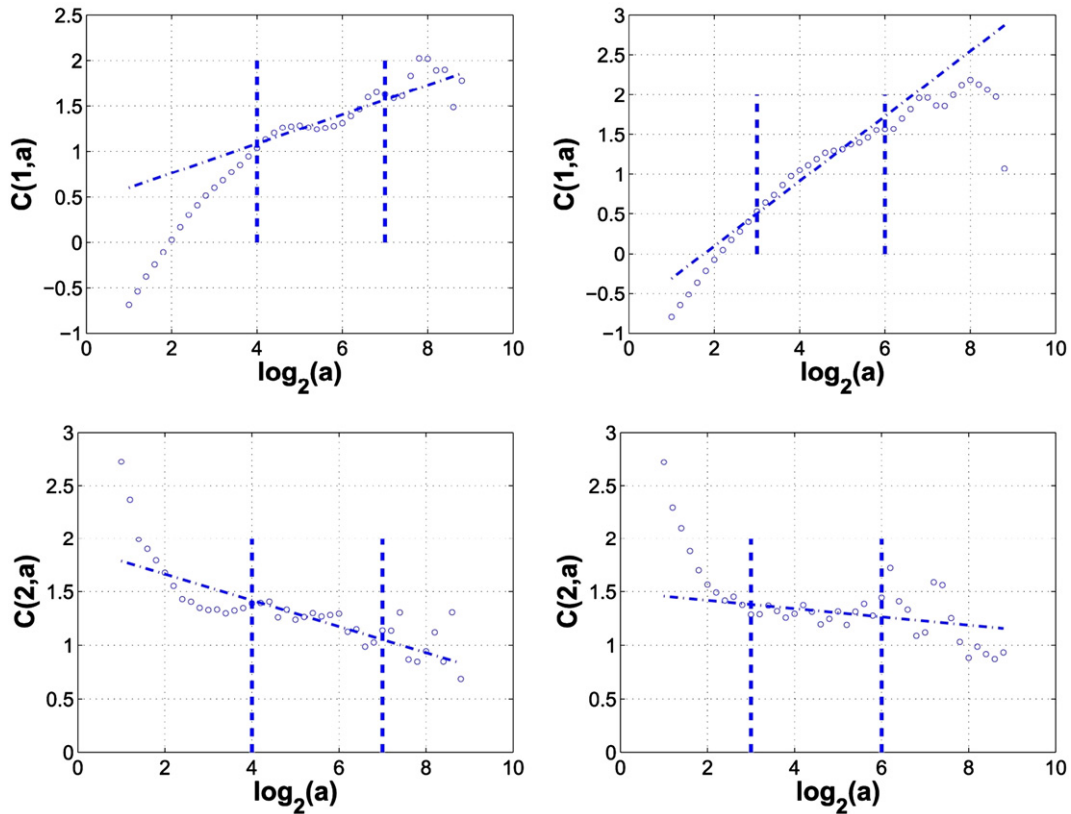


Fig. 13. Same as Fig. 12 for the river reach of 20–28 km.

one can notice a higher degree of dissection in the left-side valley. Also, it is noted that spectral analysis of the left and right corridor widths for this segment (Fig. 7) was not able to depict the subtle differences depicted by MF analysis.

6. Discussion and conclusions

The goal of this work was to examine the multiscale statistical properties of the river corridor width (RCW) series along the mainstream of a 35 km mountainous channel reach with the goal of assessing whether the valley forming processes imprint on this series any particular statistical organization.

Some clear results have emerged from this analysis. First, river corridor width fluctuations exhibit a rich multiscale statistical structure and a deviation from scale-invariance or monoscaling. Second, as one goes further away from the outlet of the basin to less steep, alluvial valleys, the statistical “roughness” of the RCW series increases (smaller c_1 or $\langle H \rangle$ values) and also the degree of multifractality, or intermittency, increases (larger c_2 values) (see Table 1). Third, for the particular

basin analyzed, a significant left-right asymmetry exists in the statistical structure of valley geometry: the left side is consistently rougher and more intermittent implying that different physical mechanisms shaped the valley at the left and right sides of the mainstream. This difference does not seem to be directly related to the number of tributaries joining the main river, as an equal number of tributaries is present on both sides of the river stretch (see Fig. 4). Rather, other mechanisms of sediment transport, landsliding, etc., seem to be the underlying cause. As we go further up to even steeper along-river slopes, no scaling is present at all, at least not in a significant range of scales, and further careful analysis needs to be undertaken.

Our analysis objectively depicted two statistically distinct regimes with transitions at around 14 km and also 28 to 35 km (see Fig. 14). An interesting question is whether these statistically distinct regimes are the result of physically distinct valley-forming processes. Another interesting question is whether the documented statistical structure of river corridor widths, which is seen as an emergent property of the physical system, can be faithfully reproduced by numerical models of landscape

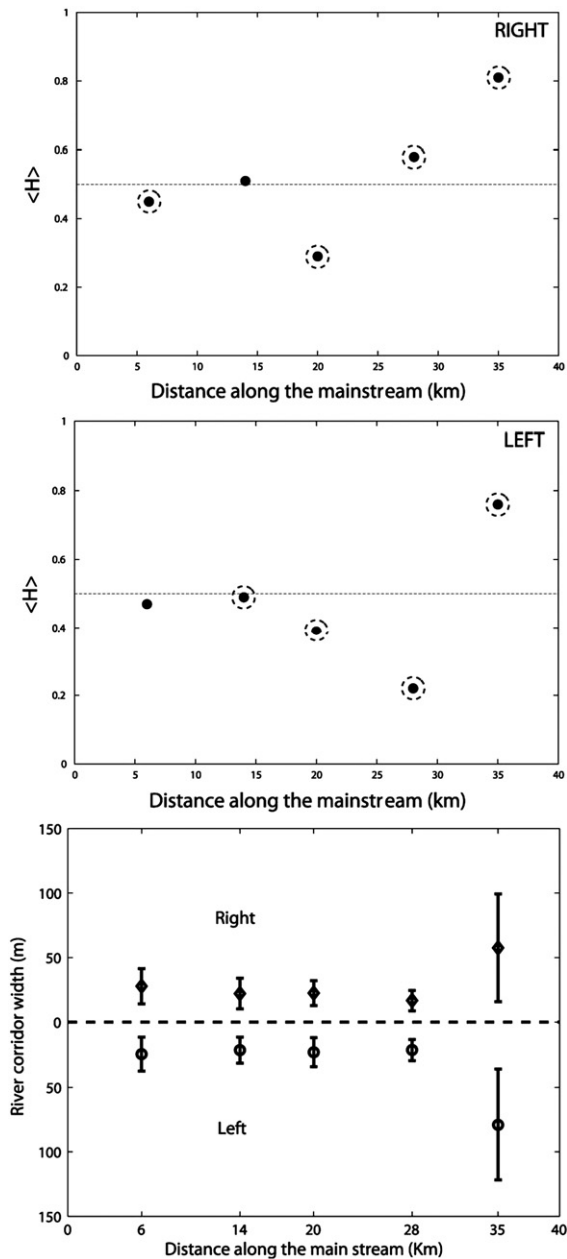


Fig. 14. Hurst exponents for the right side (top) and left side (middle) RCW series (at $D_0=5$ m). Larger values of $\langle H \rangle$ indicate “smoother” signals. Points with circles around them indicate reaches with a significant deviation from monoscaling (large c_2 values (see Table 1)). The bottom panel shows the mean of the RCW series ± 1 standard deviation for each of the five segments. Note that the dramatic increase of the variance for the 28–35 km segment comes from large-scale features (see Fig. 4) and not from very abrupt high frequency (small scale) fluctuations, as this segment exhibits a very smooth fractal structure (see the large $\langle H \rangle$ in top two panels).

evolution at the hillslope scale (e.g., see Roering et al., 1999). Both of these questions are the subject of future investigations.

Acknowledgements

We thank Dino Bellugi and Collin Bode for providing us with the data, and Stéphane Roux (Laboratoire de Physique, École Normale Supérieure de Lyon, Lyon, France) for help in implementing the WTMM methodology. Discussions throughout the course of this work with William Dietrich and Bruno Lashermes are greatly appreciated. This work has been partially supported by the National Center for Earth-surface Dynamics (NCED), a Science and Technology Center funded by NSF’s Office of Integrative Activities under agreement EAR-0120914. Computer resources were provided by the Minnesota Supercomputing Institute, Digital Technology Center, at the University of Minnesota. The constructive comments of Jon Pelletier and Brad Murray are gratefully acknowledged.

References

- Arneodo, A., Bacry, E., Muzy, J., 1995. The thermodynamics of fractals revisited with wavelets. *Physics A* 213, 232–275.
- Arneodo, A., Bacry, E., Jaffard, S., Muzy, J., 1998. Singularity spectrum of multifractal functions involving oscillating singularities. *J. Fourier Anal. Appl.* 4, 159–174.
- Barenblatt, G.I., 2003. *Scaling*. Cambridge University Press, Cambridge. 186 pp.
- Delour, J., Muzy, J., Arneodo, A., 2001. Intermittency of 1d velocity spatial profiles in turbulence: a magnitude cumulant analysis. *Eur. Phys. J., B Cond. Matter Phys.* 23, 243–248.
- Jaffard, S., 1989. Exposants de Hölder en des points donnés et coefficients d’ondelettes. *C. R. Acad. Sci., Ser. I Math.* 308, 79–81.
- Kolmogorov, A.N., 1941. The local structure of turbulence in incompressible viscous fluid for very large Reynolds number. *Dokl. Akad. Nauk SSSR* 30, 299–303.
- Lashermes, B., Foufoula-Georgiou, E., 2007. Area and width functions in river networks: new results on multifractal properties. *Water Resour. Res.* 43. doi:10.1029/2006 WR005329.
- Mahrt, L., 1989. Intermittency of atmospheric turbulence. *J. Atmos. Sci.* 46, 79–95.
- Mallat, S., 1998. *A Wavelet Tour of Signal Processing*. Academic Press, San Diego, CA.
- Mallat, S., Hwang, W.L., 1992. Singularity detection and processing with wavelets. *IEEE Trans. Inf. Theory* 38, 617–643.
- Montgomery, D., 2002. Valley formation by fluvial and glacial erosion. *Geology* 30 (11), 1047–1050.
- Muzy, J., Bacry, E., Arneodo, A., 1991. Wavelets and multifractal formalism for singular signals: application to turbulence data. *Phys. Rev. Lett.* 67, 3515–3518.
- Muzy, J., Bacry, E., Arneodo, A., 1993. Multifractal formalism for fractal signals: the structure-function approach versus the wavelet-transform modulus-maxima method. *Phys. Rev., E Stat. Phys. Plasmas Fluids Relat. Interdiscip. Topics* 47, 875–884.
- Muzy, J., Bacry, E., Arneodo, A., 1994. The multifractal formalism revisited with wavelets. *Int. J. Bifurc. Chaos Appl. Sci. Eng.* 4, 245–302.
- Parisi, G., Frisch, U., 1985. On the singularity structure of fully developed turbulence. In: Frisch, U. (Ed.), *Proc. Int. Summer school Phys. Enrico Fermi*, North Holland.

- Power, M., 1992. Hydrologic and trophic controls of seasonal algal blooms in northern California rivers. *Arch. Hydrobiol.* 125, 385–410.
- Roering, J., Kirchner, J., Dietrich, W.E., 1999. Evidence for nonlinear, diffusive sediment transport on hillslopes and implications for landscape morphology. *Water Resour. Res.* 35 (3), 853–870. doi:10.1029/1998WR900090.
- Seidl, M., Dietrich, W., 1992. The problem of channel erosion into bedrock. *Catena* 23 (Supplement).
- Venugopal, V., Roux, S., Foufoula-Georgiou, E., Arneodo, A., 2006a. Revisiting multifractality of high-resolution temporal rainfall using a wavelet-based formalism. *Water Resour. Res.* 42 (6), W06D14. doi:10.1029/2005WR004489.
- Venugopal, V., Roux, S.G., Foufoula-Georgiou, E., Arneodo, A., 2006b. Scaling behavior of high resolution temporal rainfall: new insights from a wavelet-based cumulant analysis. *Phys. Lett., A* 348, 335–345.